Available online at www.sciencedirect.com

ScienceDirect

Energy Procedia 4 (2011) 3676–3683

Energy Procedia

www.elsevier.com/locate/procedia

GHGT-10

Integration of core sample velocity measurements into a 4D seismic survey and analysis of SEM and CT images to obtain pore scale properties.

Alan Mur[1,2], Christopher Purcell[1,2], Yee Soong[1], Dustin Crandall[3], T. Robert McLendon[1], Igor V. Haljasma[3], Robert Warzinski[1], Barbara Kutchko[1], Stephen Kennedy[4] , William Harbert[1,2]

[1] *National Energy Technology Laboratory, United States Department of Energy, Pittsburgh, PA.*
[2] *Department of Geology and Planetary Science, University of Pittsburgh, Pittsburgh, PA.*
[3] *URS Corporation, National Energy Technology Laboratory, Pittsburgh, PA.*
[4] *RJ Lee Group, Monroeville, PA.*

Abstract

The Scurry Area Canyon Reef Operators Committee (SACROC) field, located in the Permian Basin of West Texas is an enhanced oil recovery (EOR) site into which large volumes of CO_2 have been injected. We acquired core samples and 3D seismic surveys from the site in order to better characterize the movement of the CO_2 injection plumes. The samples of SACROC reef limestone were used for ultrasonic velocity measurements, detailed mineralogy and Scanning Electron Microscopy (SEM) characterization, Computed Tomography (CT) scanning, thin section studies, and porosity measurements. Using a NER AutoLab 1500 at the National Energy Technology Laboratory (NETL) Core Flow Lab we have measured P and S wave velocities, porosity, and permeability at varying pressures, temperatures, and fluid saturations that simulate reservoir conditions after successive floods. Measurements were also taken with supercritical CO_2 at *in situ* pressures and temperatures. We also modeled the expected velocities for our samples using the standard Gassmann and other rock physics. We created a tool that groups grayscale ranges into three categories, cleans boundaries between groups, and produces a polygon map of the macropores, micropores, mineral grains, and matrix. In addition, the CT and SEM pore maps were analyzed to reveal pore shape statistics. Pore volume, area, and connectivity is essential for chemistry experiments that will emulate time exposure of CO_2 to limestone. Further, this analysis technique allows us to obtain pore orientation information, which is important in understanding the anisotropic conditions that may affect seismic data. This multi-scale approach can help to characterize what is occurring inside of the reservoir. Fine scale measurements of how CO_2 affects pore-space dissolution can help to inform us of any changes in overall reservoir storage capacity due to changing porosity. Core-scale velocity

doi:10.1016/j.egypro.2011.02.299

measurements under *in situ* conditions will allow us to predict changes in future well log or seismic surveys. Combining microscale, mesoscale, and macroscale information should lead to a better understanding of the various processes at work when CO_2 is sequestered in a limestone reservoir.

Keywords: Carbon Sequestration; Rock Physics; Pore Scale Properties; CT Characterization; ImageJ; 4D Seismic; SEM Image Analysis; AVO

Introduction

The Scurry Area Canyon Reef Operators Committee (SACROC field), located in north central Texas in the Permian Basin, is the oldest CO_2 enhanced oil recovery site in the United States, with over 86.2 million tons of CO_2 purchased as of 2010. Recently the National Energy Technology Laboratory (NETL) of the United States Department of Energy has begun to support an enhanced oil recovery project at the SACROC field in north central Texas in close collaboration with the Bureau of Economic Geology in Austin, Texas involving the injection of CO_2 at a depth of approximately 6700 ft (2042 m) into a reef structure.

The NETL Geological Sequestration Core Flow Laboratory (CORFLO) is a flexible, state-of-the-art facility investigating solutions for how to store CO_2 that has been captured from various sources. For rock physics studies, the laboratory includes a New England Research (NER) AutoLab 1500 computer-controlled servo hydraulic triaxial test system that can measure permeability with H_2O, CO_2 (liquid, super-critical, and gas phases), and brine; pore-volume compaction (volume or storage); Young's modulus; Poisson's ratio; and stress/strain relationships via strain gages and linear variable differential transducers. P-wave ultrasonic wave velocity and SH and SV ultrasonic wave velocities are measured using transducer heads operating at a frequency of 500–700 kHz.

Core Preparation

Two large core samples of the SACROC Limestone were provided by Kinder Morgan and the Bureau of Economic Geology. A 2 in (5.08 cm) diameter sample was taken from each core. Core #1 comes from a depth of approximately 6500 ft (1981 m), while core #2 comes from a depth of 6180 ft (1884 m) below the surface. Core #1 has a bulk density of 2.200 g/cm^3 and a length of 2.85 in (72.35 mm), while core #2 has a Bulk Density of 2.550 g/cm^3 and a length of 2.69 in (68.28 mm). In addition, samples of Berea Sandstone were measured as a known reference material. The cores were tested in a Temco Helium Porosimeter. Core #1 had a porosity of 19%, while core #2 had a porosity of 6.6%.

We used a 4 inch diameter oriented sample from core #2 for the three-plane characterization and subset our core #1 as needed for our Computed Tomography (CT) and Scanning Electron Microscopy (SEM) mosaic studies. For rock velocity measurement samples, a large drill press with cooling water was used to core the samples, and a water cooled diamond saw was used to square off the ends of the cores. After drying the samples in a desiccator jar, they were then measured and weighed, resulting in the weights mentioned in the previous paragraph.

SEM and CT Characterization

SEM and X-Ray Diffraction analysis revealed a vuggy carbonate with stylolites and abundant ammonoid bioclasts composed of >80% calcite, variable amounts of dolomite, quartz, apatite, and clay minerals. We wanted to develop a method that would calculate pore count, orientation, and physical dimensions of pores in an SEM image. We used ArcGis and Fiji (a build of the ImageJ processing software) on an SEM montage composed of 20 images across and 22 images down. Each image was 512 x 512 pixels and acquired at 200x with a scale of 0.86816 μm per pixel. The overall size of the analyzed SEM montage was 0.35 x 0.39 in (8.89 x 9.78 mm).

An analysis tool was designed to classify the grayscale intensity into three classes: Dark, cave like structures fell between 0-75 and we classified as macro porosity. Continuous matrix fell in the 75-116 range. Bright, energy-scattering textural features from 116-255 were defined as micro porosity. The class layer was simplified with a boundary clean operation. Then, polygons were drawn around the groups of similarly classed pixels, creating a polygon map of macro/micro pores and matrix. Since the macro pore class includes many small

vugs and comparatively fewer large vugs, the macro pore perimeter data was divided into the low varying small vugs, and larger vugs. A perimeter length of greater than 11.25 microns was chosen as the dividing line between small and large vugs because there is limited variation in pore perimeter at low pixel values. This value was also chosen because it is the mean perimeter length.

This tool effectively became a matrix-pore boundary texture analysis method. It revealed that in our sample, we had low macro-porosity (6%) and high micro-porosity values (57.5%) which we sub-divided into matrix and actual porosity to balance our porosimeter measurements. Micro-porosity has a higher surface area to volume ratio than that of the macro pores. This has implications for both chemical models that require surface area values for rate of reaction modeling as seen in Khinast et al. [1] as well as sonic velocity values related to micro vs. macro pore percentages, as described by Baechle et al. [2].

After the analysis method was developed on the initial sample, further samples were taken from core #2. These samples were cut perpendicularly to check for obvious orientation characteristics. We refined our methodology in accordance with Stutzman et al. [3] findings on epoxy impregnation. Hardened epoxy improves contrast between pore space and matrix, strengthens the microstructure, and improves its ability to withstand mechanical preparation without fracturing, plucking out mineral grains, or filling voids with debris [3]. We used the services of RJLee Group (Monroeville Pennsylvania, USA) to have the core further analyzed. The mutually perpendicular, epoxy impregnated, polished samples (2 40mm x 45mm samples and 1 80mm x 40mm sample) were produced from a core column and analyzed using a Keyence digital microscope for optical and an Aspex Personal SEM 75 for scanning electron microscopy. The analysis produced an optical montage, a backscattered electron SEM (BSEM) montage, a CCSEM (computer controlled scanning electron microscope) point count analysis and a CCSEM High-Z analysis.

High-Z analysis characterizes particles that are larger than 0.2 μm and are brighter than the matrix in the BSEM image (where brightness is proportional to average atomic number). The report revealed the presence of trace amounts of phosphorus, sulphur, titanium, vanadium, chromium, iron, nickel, copper, strontium, zircon, and barium.

The classification system we developed for epoxy impregnated SEM images was slightly different than our original method. Once impregnated, samples no longer exhibit the depth or dimensionality that un-impregnated polished samples have. In this scheme, the darkest points are both macro and micro pores. There are two grayscale peaks: one at about 35 and one at about 100. The classes are 0 - 55, 56 - 100, and 101 - 255. This classification accounts for mineralogy in that there are two matrix classes that define calcite and dolomite grains. The darkest pixel (pore) class is selected and a subset raster is created. This raster data is then converted to polygons. The polygons with area values greater than 130 square microns are chosen because lesser values approach minimum pixel limits for shape analysis.

This polygon set is then converted back into a raster and then into a .tiff file and loaded into Fiji. Once in Fiji, the .tiff is thresholded and using the particle analysis tool we find area, size, axis length, orientation, circularity, and solidity of individual pores. Individual pores and average pore statistics were determined.

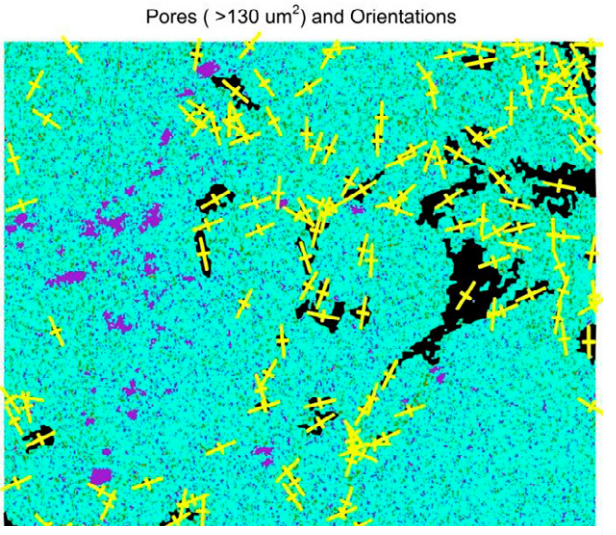

Figure 1 Pore, matrix, and light grains (black, aqua, purple respectively) with pore orientations overlain in yellow.

We acquired a CT dataset at 10x zoom at 2.242 μm/pixel resolution from an XRadia-400 Micro-XCT scanner. Select slices from the set were analyzed with the ArcMap tool. We classified the grayscale into three categories: pore, matrix, and bright grains, converted the classes to polygons and exported the pore class as a binary image. Using Fiji to analyze the pore image, ellipsoids were best fit around the pores and a dataset with values for spatial location, area, major/minor axis lengths, angle of major axis from x-axis, aspect ratio, and solidity for 165 pores was produced. We imported the data back into ArcMap and produced a map with the three classifications and the orientation of each pore (Figure 1). The rose diagram of pore orientation reveals two preferred orientations of the larger pores and a preferred orientation of the smaller pores (Figure 2).

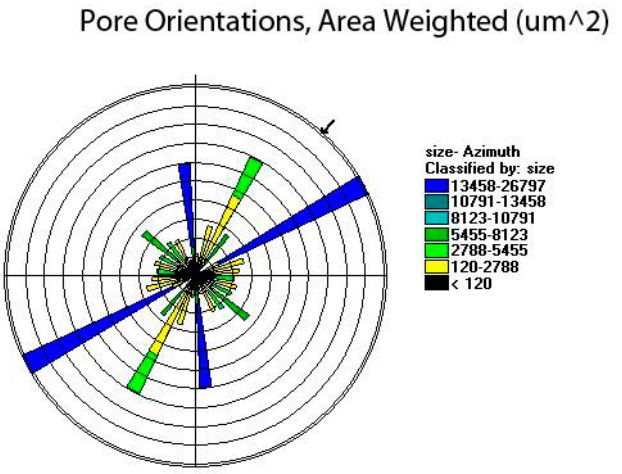

Figure 2 Rose diagram depicting pore orientations in a 2-D slice weighted by area

We cropped the entire CT dataset with Fiji, to a 686 x 626 x 499 pixel (1.54 x 1.40 x 1.12 mm) data set and ran the 3-D Object Counter plug-in. This plug-in finds user defined minimum groupings of pixels in each slice of the stack, groups them with neighbouring groups in above and below slices, and associates touching groups through the volume [4][5]. Run time of this analysis took over twelve hours with a 2.67 GHz Intel i7 CPU with 7 GB of RAM allocated to the processing program. This tool produces pore volume, surface area, volume coordinates, bounding box dimensions, centroid/center of mass and associated distances to pore surfaces. The colorized numbered pores through the volume allow visual aid in understanding pore connectivity. Figure 3 shows a large network of pores in white and unconnected pores in red.

Using the volume analysis and previously measured values for density and porosity, we find that core #1 has 175 cm^2 of pore surface area per gram between the pore volume sizes from $2.8*10^2$ μm^3 to $2.8*10^8$ μm^3.

Statistically, of the 11,089 pores analyzed, volume distribution grows to 500 μm^3 and then decrease exponentially. A large connected pore network exists in the sample and produces outlying large volume values.

Our study consisted of three scales of characterization. The first SEM mosaic shows the texture and dimensionality of pores and the need to account for both micro and macro porosity. The RJ Lee with High-Z analysis study revealed high resolution chemical composition as well as more accurate 2-D pore information. At centimetre-size x,y dimensions, these two SEM analysis produced large 2-D pore datasets with more than 20,000 pore descriptions in each set.

The CT set has the most data at the highest zoom level. It most accurately displays pore volumetrics and orientations, but does not contain the elemental information that can be provided by the High-Z analysis.

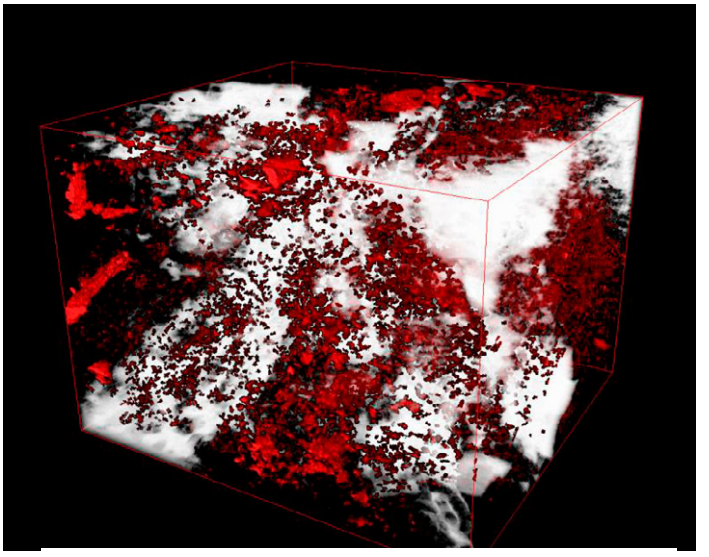

Figure 3 Large connected pore network shown in white and unconnected pores in red. (Volume size 1.54 x 1.40 x 1.12 mm)

Numerical Flow Simulation from CT Scans

A portion of the large connected pore network shown in Figure 3 was isolated, converted to a numerical mesh, and used to perform a pore-level computational fluid dynamics (CFD) simulation. The numerical simulation was performed with the commercial CFD software ANSYS FLUENT, which solved the discretized Navier-Stokes equations of fluid motion on a finite volume grid, assuming laminar flow and no slip walls to the pore space. The isolated region of the pore network is shown in Figure 4(A) as the region in blue, which has a volume of 6.2 (10^6) voxels or 0.014 mm^3. This region was isolated with ImageJ and exported as a mesh to the visualization software Amira. This mesh was smoothed and refined using standard image processing techniques and exported as a boundary surface in FLUENT mesh format. The boundary mesh was used to generate a volumetric grid of 42,966 cells with the meshing software TGrid. This mesh is shown in Figure 4(B), with the blue plane at the top of the mesh a velocity inlet boundary and the red plane at the bottom a fluid outflow boundary. This mesh was used in FLUENT to model the flow of water through the entire domain when entering perpendicular to the inlet with a velocity of $1^{cm}/_{s}$. As is shown by the velocity vectors in Figure 4(C) the majority of the flow in the domain was much less than $1^{cm}/_{s}$. By cropping the velocities to the 0.05 to 0.0012 $^{m}/_{s}$ the primary flow path through this segment was identified (Figure 4(D)), with faster flow shown in small channels along this percolation backbone. The largest velocity vectors at the outlet of Figure 4(C) are due to recirculation and are an artefact of the non-physical boundary condition. The two findings of fastest flow through smallest restrictions in the pore network and near-stagnant flows away from the percolation backbone are expected to be found in larger CFD simulations in the CT scanned pore space, which are under development at the time of this writing.

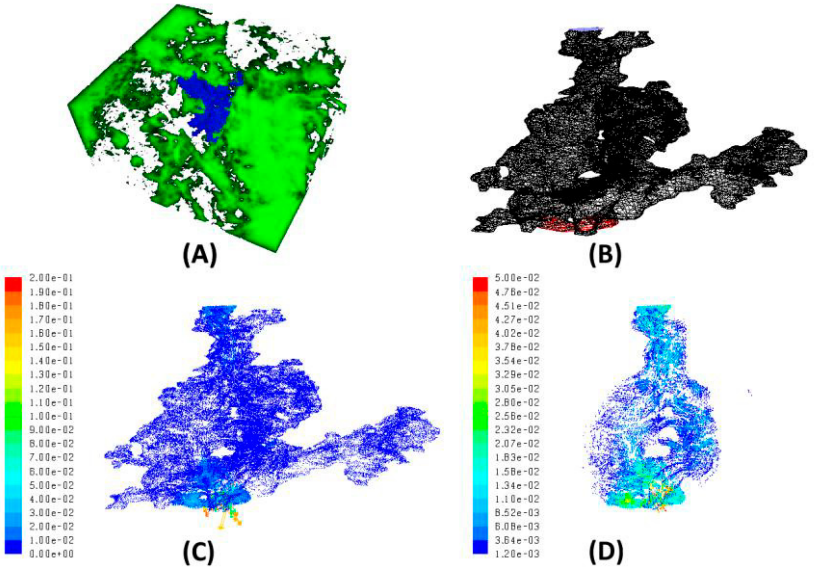

Figure 4 Computational Fluid Dynamics simulation through a segment of the pore domain (A) the isolated connected pore space, shown in blue (B) the meshed flow domain (C) velocity vectors of water flow and (D) cropped range of velocity vectors, showing the primary flow path through the CT scan derived domain. Velocity vector legends in $^{m}/_{s}$.

Velocity Experimental Setup

For our velocity measurements, we used a New England Research (NER) AutoLab 1500. It is capable of generating variable confining and pore pressures on 1, 1.5, and 2 inch diameter cores up to 70 MPa. After preparing our cores, they are placed inside of a jacket in order to separate the confining oil pressure and the internal pore pressure of the sample. The jacketing material used in our experiments is Buna-N, which was used to retard the adsorption of CO_2 into the jacket. The inside diameter of the jacketing rubber is the same as the outside diameter of the core sample. It is cut longer than the sample in order to fit over the specimen support pedestal on the transducer heads. The jacket is then secured in place using steel wire. Making sure that the two transducers are lined up to have the same shear wave polarization direction, the second transducer is secured to the core. The sample is then placed inside of the pressure vessel and experiments are performed.

The coreholders used are capable of measuring one compressional (V_p) and two orthogonally polarized shear waves (V_{sh}, V_{sv}), at an operational frequency between 500 and 700 kHz. The velocity heads were connected to

an oscilloscope, which is controlled by the NER software package running on an external computer. After adjusting the confining pressure, pore pressure, and temperature to the desired values, the raw traces were collected from the oscilloscope. The original arrival times of each waveform were selected using the NER software package. These times were used in conjunction with a correction factor to automatically calculate our velocities. The correction factor allows us to subtract out the additional time needed for the wave to pass through the core holders and was derived by attaching the core holders to one another with no sample in place between them.

Rock Velocity Experiments

We conducted several different types of tests on the Core #1 reservoir sample. We first ran experiments where the confining pressure was incrementally raised up to 50 MPa. A marked increase in P-Wave velocity was seen, indicating the closure of microcracks in the sample [6]. We then flooded the cores with CO_2 under different temperature/pressure conditions, which included gaseous, liquid, and supercritical phases. In-situ temperature conditions were replicated through the use of a heating element built into the AutoLab unit. We varied the pore pressure of the sample between 0 and 30 MPa while maintaining a constant confining pressure of 30, 40, and 50 MPa. Increasing pore pressure caused the velocity to decrease rapidly under all confining pressure regimes [7]. This agrees well with other studies [8].

We also completed hysteresis experiments on a CO_2 saturated sample. It showed little velocity change between pressurization and depressurization at the low effective pressures associated with our reservoir [7]. We also completed a higher resolution hysteresis experiment where only confining pressure was changed, and no pore fluids were introduced into the sample. The pressure was varied between 3 and 50 MPa in increments of 1 MPa, and then depressurized in the same way. Between each confining pressure increase, the sample was allowed to equilibrate for 5 minutes before measurements were made. At high pressures, the velocities agreed well, but at low confining pressures, the velocities on the depressurization curve were found to be higher by ~5%.

Gassmann Calculations

We calculated the expected velocities for our samples using the standard Gassmann equations and the Mavko-Jizba equations [9][10]. We then used the Generalized Mavko-Jizba equations given in Gurevich et al., which correct for gas saturated rocks (Figure 4) [11]. The calculated results were then compared with our experimental results of CO_2 saturated SACROC material at 50°C, and found good agreement with both the Mavko-Jizba and Gurevich equations at high effective pressures [7].

The Gassmann, Mavko-Jizba, and Gurevich equations were used. The differences between the three methods for the SACROC limestone are significant. The Gassmann equations give lower velocity predictions than the Mavko-Jizba equation except for low effective pressures corresponding to a gaseous phase. The Mavko-Jizba and Gurevich equations give the same results at higher effective pressures, but the Gurevich generalized version of the equation is more accurate at low effective pressures, due to the low bulk modulus of gaseous CO_2[11].

$$\frac{1}{K_{uf}(P)} = \frac{1}{K_h} + \frac{1}{\dfrac{1}{\dfrac{1}{K_{\mathrm{dry}}(P)} - \dfrac{1}{K_h}} + \dfrac{1}{\left(\dfrac{1}{K_f} - \dfrac{1}{K_g}\right)\phi_c(P)}},$$

Equation 1: Generalized Mavko-Jizba equation from Gurevitch et al [11].

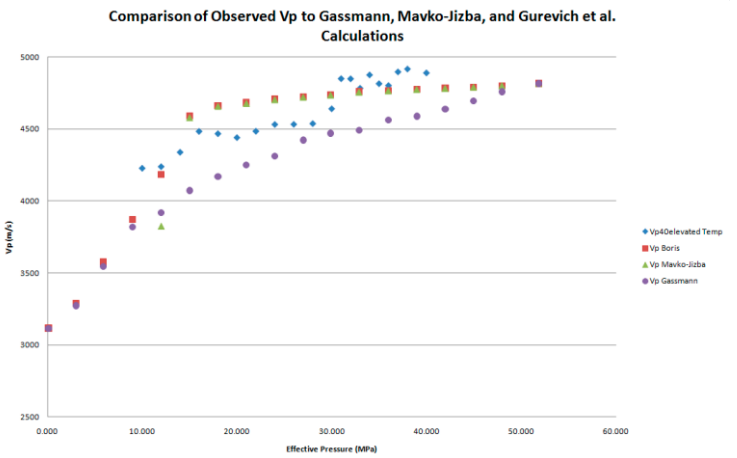

Figure 5 Comparison of Gassmann, Mavko-Jizba and Gurevich et al. Calculations to CO_2 saturated limestone.

Anisotropy

Seismic anisotropy is the variation of velocity with direction, and is an indicator of alignment of features that are smaller than the seismic wavelength, such as cracks, pores, or layers, leading to a directional variation in seismic velocity. Anisotropy experiments were performed on two cores of widely differing porosity (6.6% vs. 19%). The experiments were porformed by rotating the core 45 degrees after each set of experiments were completed. Four sets of measuremtnts were completed at 0, 45, 90 and 135 degrees, and confining pressure was varied from 5-60 MPa for each run, with no saturating fluid. Core #1, which has a porosity of 19%, is from a depth of 6500 ft, and core #2, which has a porosity of 6.6%, was from a depth of 6180 ft.

The results of these experiments show that while core #1 has only a slight variation in velocity ~1-3%, core #2 has an S-Wave Anisotropy of up to 10%, indicating the strong orientation of rock matrix features, perhaps vugs (Figure 6).

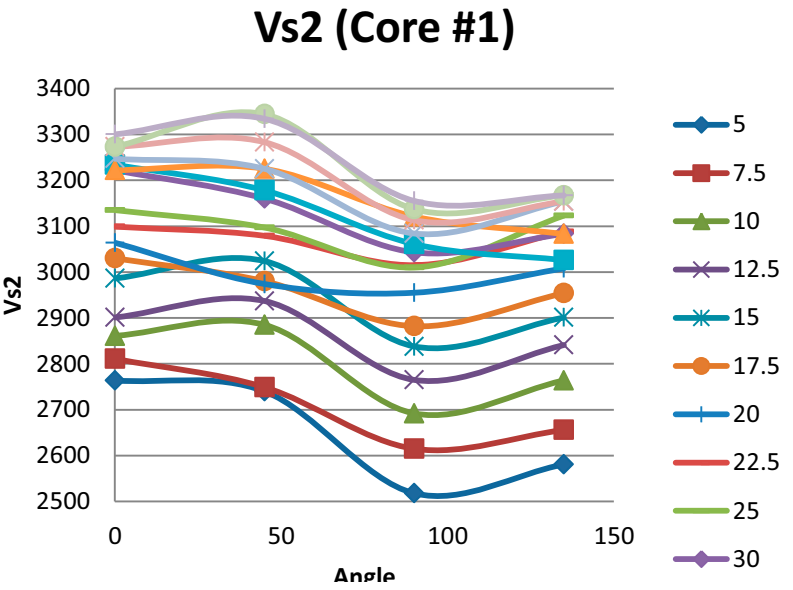

Figure 6 S2 Anisotropy in Core #1

Resistivity

The DOE has recently aquired a resistivity measurment system for the AutoLab 1500, which allows for 2 or 4 electrode resistivity measurements as a function of frequency, stress, and temperature. This configuration can take measurements at frequencies from 0.02 Hz to 200,000 Hz.

A tap water saturated core was tested first, so see if any pressure dependent resistivity could be found. The sample was saturated with tap water, and the confining pressure was varied from 5-60 MPa. We found a strong dependence of resistivity on pressure; the resistivity of the sample increased 81% over the pressure range. This

increase in resistivity is due to the closing of microcracks, and the cutting off of paths for conductive ion transport. Future experiments will be conducted on Brine and CO_2 saturated samples.

Conclusions

Our method of predicting the location of injected CO_2 in the reservoir is becoming more accurate as we update our model from the micro-scale up to the macro-scale. Our velocity measurements serve as a test of different rock physics models. Velocity models are more complex and allow for the incorporation of micro-macro pore differentiation, compliant (soft) porosity, and the phase of the pore-filling substance. Our velocity measurements show a marked decrease of velocity when CO_2 is introduced into the pore space. This decrease is large enough to be detectable in a seismic survey, assuming the concentration is high enough. Our CT and SEM investigation has produced pore surface and volume values that can be used for chemical modelling as well as pore orientation values that can be used for velocity anisotropy analysis. In addition, it provides a measure of pore size ranges, and also allows us to determine the relative fractions of micro- and macro-porosity.

References

[1] J. Khinast, G. F. Krammer, Ch. Brunner and G. Staudlinger . Decomposition of limestone: The influence of CO2 and particle size on the reaction rate. Chemical Engineering Science 51(4), 1996; 623-634.
[2] G.T. Baechle, A. Colpaert, G.P. Eberli and R.J. Weger. Effects of Microporosity on Sonic Velocity in Carbonate Rocks. The Leading Edge, August 2008; 1012-1018.
[3] P.E. Stutzman. Specimen Preparation for Scanning Electron Microscopy, the Twenty-First International Conference on Cement Microscopy; April 25-29, 1999.
[4] M.D. Abramoff, P.J. Magelhaes and S.J. Ram. Image Processing with ImageJ. Biophotonics International 2004; Vol. 11: No. 7:36-42.
[5] S. Bolte and F.P. Cordelieres. A guided tour into subcellular colocalization analysis in light microscopy. Journal of Microscopy, Vol. 224, Issue 3: 213-232.
[6] S. Shapiro and A. Kaselow. Porosity and elastic anisotropy of rocks under tectonic stress and pore-pressure changes. Geophysics 2004; Vol. 70 No. 5:N27-N38.
[7] C. Purcell, A. Mur, Y. Soong, T.R. McLendon, I.V. Haljasmaa and W. Harbert. Integrating velocity measurements in a reservoir rock sample from the SACROC unit with an AVO proxy for subsurface supercritical CO2. The Leading Edge 2010; 29, 192.
[8] Z. Wang and A. Nur. Effects of CO_2 flooding on wave velocities in rocks with hydrocarbons. SPE Reservoir Engineering, 1989; 429-436.
[9] F. Gassmann. Elastic Waves Through a Packing of Spheres. Geophysics 1951; 673.
[10] G. Mavko and D. Jizba. Estimating grain-scale fluid effects on velocity dispersion in rocks. Geophysics 1991; 1940-1949.
[11] B. Gurevich, D. Makarynska and M. Pervukhina. Ultrasonic moduli for fluid-saturated rocks: Mavko-Jizba relations rederived and generalized. Geophysics 2009; Vol. 74, No. 4:N25-N30.

Acknowledgements

This technical effort was performed in support of the National Energy Technology Laboratory's on-going research in rock physics and seismic imaging of subsurface CO_2 under the RDS contracts 606.08.05.201 and 606.08.05.202. We wish to thank Dr. Bob Hardage, Dr. Diana Sava and Ms. Rebecca Smyth of the Bureau of Economic Geology and the Southwest Regional CO_2 Partnership for their help and support in this project. We also wish to thank Ms. Renee Robertson, Mr. Stephen Boger and Mr. Merle Steckel of Kinder Morgan for generously allowing us access to the SACROC core material and helpful discussions. Dr. Greg N. Boitnott of NER was very helpful answering many questions regarding the AutoLab and associated software derived parameters; his patience with our questions and insight are also greatly appreciated.